

Sub-60 mV/decade switching in a metal-insulator-metal-insulator-semiconductor transistor without ferroelectric component

Peng Wu^{1,2}, Joerg Appenzeller^{1,2*}*

¹Birck Nanotechnology Center, Purdue University, West Lafayette, Indiana 47907, USA

²Department of Electrical and Computer Engineering, Purdue University, West Lafayette, Indiana 47907,
USA

*E-mail: wu936@purdue.edu, appenzeller@purdue.edu

Abstract:

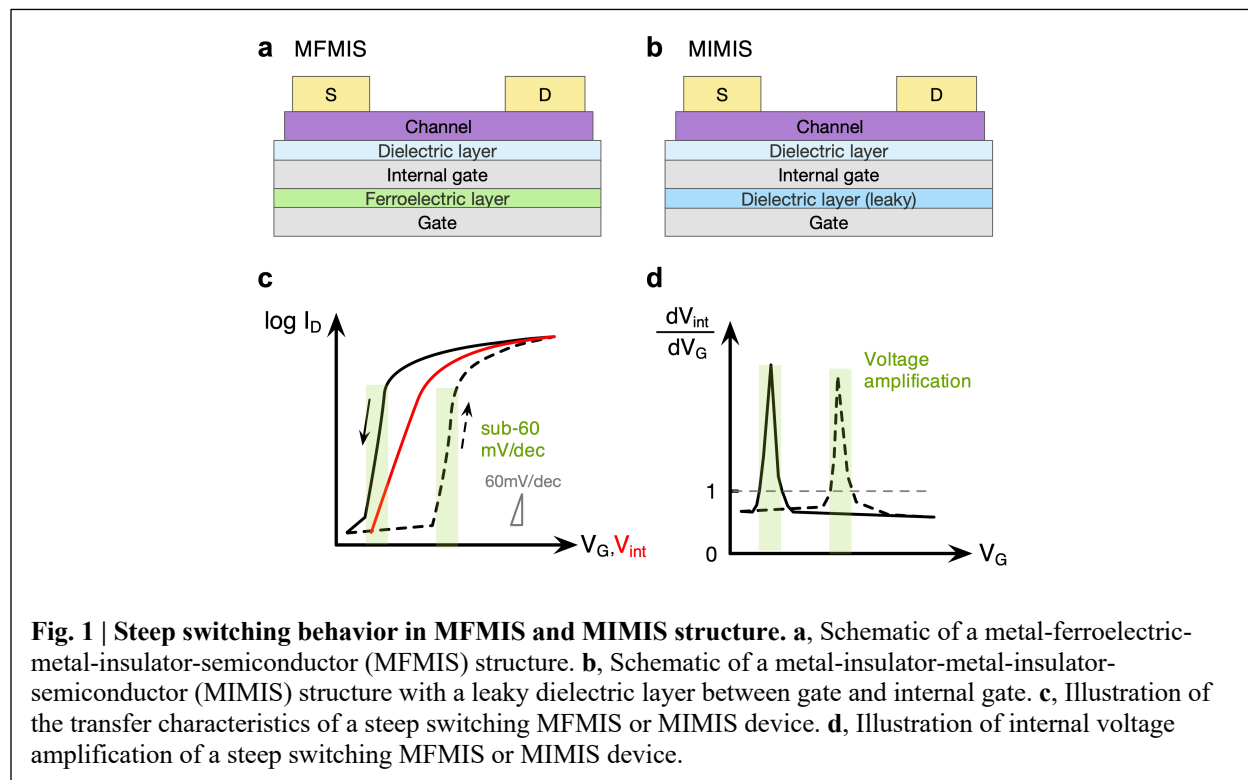
Negative capacitance field-effect transistors (NC-FETs) have attracted wide interest as promising candidates for steep-slope devices, and sub-60 mV/decade switching has been demonstrated in NC-FETs with various device structures and material systems. However, the detailed mechanisms of the observed steep-slope switching in some of these experiments are under intense debate. Here we show that sub-60 mV/decade switching can be observed in a WS₂ transistor with a metal-insulator-metal-insulator-semiconductor (MIMIS) structure – without any ferroelectric component. This structure resembles an NC-FET with internal gate, except that the ferroelectric layer is replaced by a leaky dielectric layer. Through simulations of the charging dynamics during the device characterization using an RC network model, we show that the observed steep-slope switching in our “ferroelectric-free” transistors can be attributed to the internal gate voltage response to the chosen varying gate voltage scan rates. We further show that a constant gate voltage scan rate can also lead to transient sub-60 mV/decade switching in an MIMIS structure with voltage dependent internal gate capacitance. Our results indicate that the observation of sub-60 mV/decade switching alone is not sufficient evidence for the successful demonstration of a true steep-slope switching device and that experimentalists need to critically assess their measurement setups to avoid measurement-related artefacts.

Negative capacitance field-effect transistors (NC-FETs) have been proposed as devices that could break the 60 mV/decade subthreshold swing (SS) limit of metal-oxide-semiconductor field-effect transistors (MOSFETs) at room temperature and achieve low-power switching¹⁻⁴. The proposed NC-FET structure includes a ferroelectric (FE) capacitor in series with a normal dielectric (DE) capacitor to stabilize the negative capacitance region in the ferroelectric material, leading to an internal voltage amplification and sub-60 mV/decade switching. Since then, sub-60 mV/decade operations have been reported in NC-FETs from various material systems and device structures⁵⁻¹⁰. However, the origin of the observed steep-slope switching is still under intense debate. Different from the original proposal, alternative mechanisms for the observed steep slope switching have been proposed and the validity of a stabilizing negative capacitance (NC) region of FE materials has been challenged¹¹⁻¹³. For example, some papers relate the observed steep switching to transient effects such as internal potential jumps^{14,15} or differential voltage amplification caused by polarization switching of FE material¹⁶⁻²², instead of a quasi-static NC effect represented as the “S”-shaped curve in the polarization–electric field (P – E) relation of FE materials^{1,23,24}. Other explanations include domain nucleation and growth in multi-domain FE materials^{15,25,26}. Yet due to the complexity of both the ferroelectric physics and the experimental systems, there has not been a single consolidated theory that can convincingly explain all the experimental findings. Therefore, a model system exhibiting similar device characteristics yet with simplified physics is highly sought after.

In this work, we experimentally demonstrate a two-dimensional tungsten disulfide (WS_2) transistor in a metal-insulator-metal-insulator-semiconductor (MIMIS) device structure, in which sub-60 mV/decade switching is observed. The device structure is similar to an NC-FET with internal metal gate, or equivalently a metal-ferroelectric-metal-insulator-semiconductor (MFMIS) structure (Fig. 1a), except that the ferroelectric (FE) layer is replaced by a leaky dielectric (DE) layer (Fig. 1b). In previous publications, negative capacitance FETs with leaky FE layers have been studied^{27,28}. However, to the best of our knowledge, there have been no discussions on the impact of leaky insulators in devices built with only DE layers and no FE layers. Also it has been reported that a lossy dielectric can be misinterpreted as

ferroelectric due to measurement artefacts²⁹, yet there have been no discussions on the implications of such artefacts for electrical devices.

In the MIMIS device, we show that several key phenomena observed in NC-FETs can be reproduced (Figs. 1c & 1d): (i) sub-60 mV/decade switching, (ii) anti-clockwise hysteresis, and (iii) internal voltage amplification. By replacing the FE layer with a DE layer, we are able to avoid the controversial discussion about polarization switching in the ferroelectric and can focus entirely on the charging dynamics inside the system, which is built with well-understood basic circuit components such as resistors (R) and capacitors (C). Using a simple RC network model, we are able to simulate the charging dynamics in the MIMIS device. Distinct device features i) through iii) from above can be readily explained as a result of the varying gate voltage scan rates due to auto-ranging of the current measurement, which could be a common issue in the characterization of steep-slope transistors. We further show that a sub-60 mV/decade switching can still be observed with a constant gate scan rate if the internal gate capacitance is voltage-dependent, highlighting the universality of the effect.



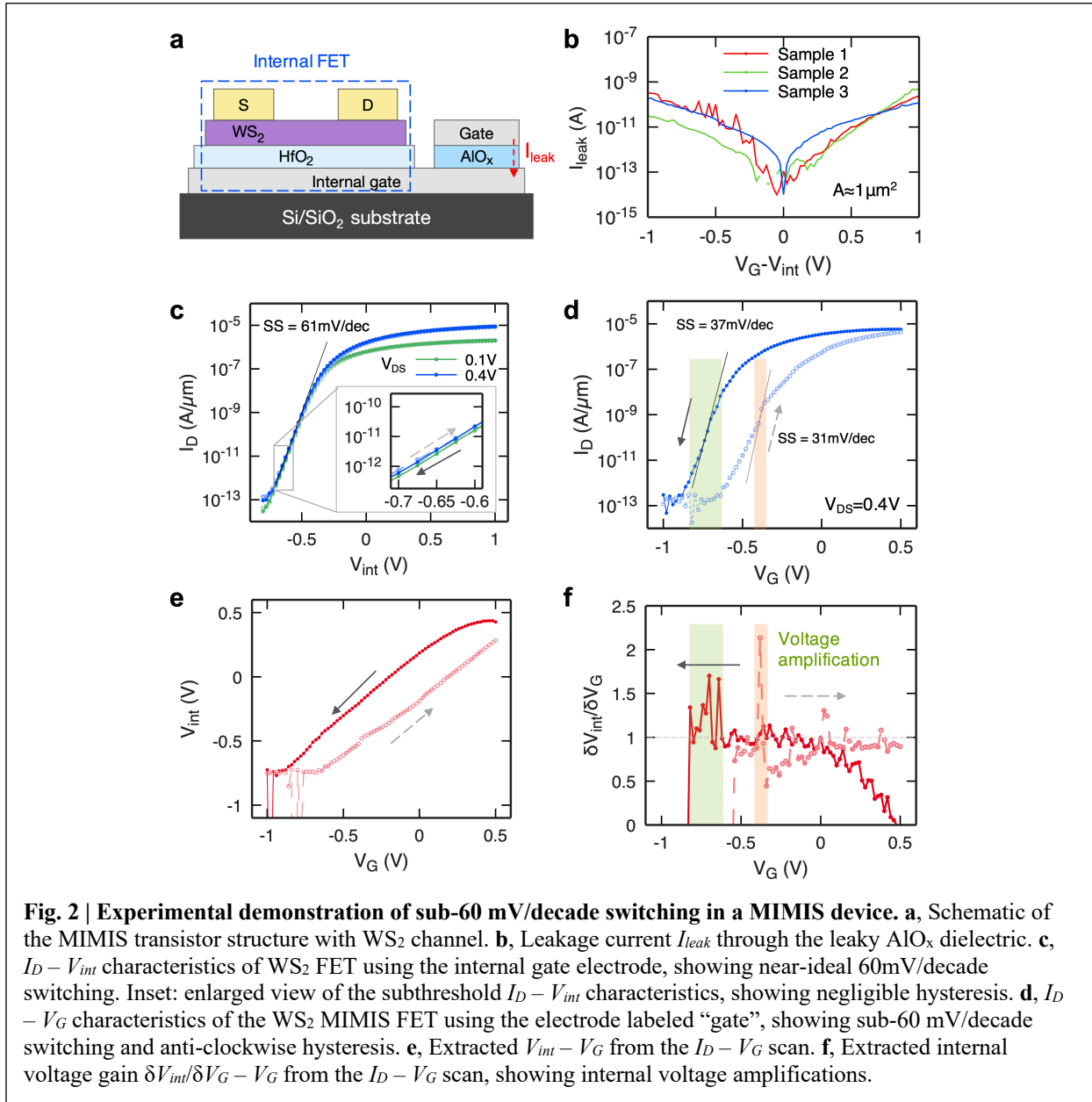
Results

Experimental demonstration of sub-60 mV/decade switching in an MIMIS device. Fig. 2a shows a schematic of the MIMIS device. The internal FET is composed of an 8-nm-thick WS₂ channel with Ni source/drain metal contacts on top of a local bottom gate structure with 7-nm-thick HfO₂ gate dielectric grown by atomic layer deposition (ALD) and Ti gate metal as “Internal gate” electrode, which is separated from the “Gate” electrode by a low-quality, leaky AlO_x dielectric film grown by natural oxidation of a thin Al layer (see Methods). The leakage current through the leaky AlO_x dielectric film in a capacitor with an area of $\sim 1 \mu\text{m}^2$ is on the order of 1~100 pA at ± 0.5 V (Fig. 2b).

Fig. 2c shows the $I_D - V_{int}$ transfer characteristics of the internal WS₂ FET. All device characterization in this study was performed using an Agilent 4156C semiconductor parameter analyzer in a LakeShore FWPX probe station at a vacuum level below 10^{-5} Torr at room temperature. Due to the ultra-thin body of the WS₂ channel and high quality of the ALD-grown HfO₂ dielectric³⁰, an SS-value of 61 mV/decade is achieved in the WS₂ internal FET, close to the 60 mV/decade room-temperature limit. Also note that the hysteresis in the $I_D - V_{int}$ characteristics of the WS₂ internal FET is negligible (inset of Fig. 2c) due to the high quality of the HfO₂ dielectric and low defect density at the semiconductor-oxide interface.

Next, we characterize the $I_D - V_G$ transfer characteristics of the WS₂ MIMIS device. As shown in Fig. 2d, an anti-clockwise hysteresis is observed in the $I_D - V_G$ characteristics, and sub-60 mV/decade switching behaviors are observed in both sweep directions, indicated by the green and orange shaded regions, respectively. The observed characteristics resemble previous reported two-dimensional (2D) NC-FETs with MFMIS device structures⁶⁻⁸, even though there is no ferroelectric component in our MIMIS device. Since the $I_D - V_{int}$ characteristics of the internal WS₂ FET are essentially hysteresis-free, we can derive a one-to-one mapping between I_D and V_{int} at a given drain voltage and extract V_{int} (Fig. 2e) and the internal voltage gain $\delta V_{int}/\delta V_G$ (Fig. 2f) during the $I_D - V_G$ scan. One can see that internal voltage amplifications

($\delta V_{int}/\delta V_G > 1$) can be observed in both sweeping directions in the $I_D - V_G$ scan. Note that although direct measurement methods of the internal gate voltage V_{int} during the $I_D - V_G$ scan exist, previous studies^{14,15} have pointed out that a voltage measurement system with input impedance much larger than the leakage resistances of the capacitors is required to accurately measure these voltages, which is not available in our measurement system. Therefore, we have adopted the strategy of indirectly extracting V_{int} from the measured I_D .



Modelling of the charging dynamics in the MIMIS device. To understand the mechanism behind the observed sub-60 mV/decade switching behaviour and internal voltage amplification in the WS₂ MIMIS device, we have performed circuit simulations of the charging dynamics during the $I_D - V_G$ scan based on an equivalent circuit model shown in Fig. 3a. In the equivalent circuit, we are considering the quantum capacitance of the WS₂ channel C_q , the oxide capacitance of HfO₂ dielectric C_{ox} , the parasitic capacitance of the internal gate to the substrate C_p , and the capacitance of the AlO_x dielectric between gate and the internal gate C_{int-G} . The leakage current in the AlO_x capacitor is modelled as a linear resistor R to simplify the discussion, although the leakage current is non-linear with voltage. Since the parasitic capacitance of the internal gate to substrate C_p is much larger than C_{ox} and C_q (see Supplementary Section 1), it is reasonable to consider only C_p and ignore C_{ox} and C_q in the simulation of the V_{int} response. The parameters used in the simulation are (Supplementary Section 1):

$$C_p = 9.59 \times 10^{-13} \text{ F}, C_{int-G} = 7.75 \times 10^{-15} \text{ F}, R = 6 \times 10^{11} \Omega$$

Next, we calculate the V_{int} response to a given V_G scan. From Kirchhoff's Current Law (KCL) at the V_{int} node, we have:

$$I_{leak} = \frac{V_G - V_{int}}{R} = \frac{d}{dt} [C_p V_{int} - C_{int-G} (V_G - V_{int})] \quad (1)$$

$$\frac{dV_{int}}{dt} = \frac{V_G - V_{int}}{R(C_p + C_{int-G})} + \frac{C_{int-G}}{C_p + C_{int-G}} \frac{dV_G}{dt} \quad (2)$$

Let $dV_{int}/dt = dV_G/dt$, we have the steady state response:

$$V_G - V_{int} = R C_p \frac{dV_G}{dt} \quad (3)$$

As indicated by Eq. (3), the difference between V_{int} and V_G at steady state is proportional to the RC time constant (which is 0.58 s for the parameters chosen here) and the V_G sweep rate (dV_G/dt), which agrees with the simulated V_{int} responses to different V_G scan rates in Fig. 3b. Now if we think about a *varying the* V_G sweep rate (“fast” to “slow”, Fig. 3c), there is a transition period (green shaded area in Fig. 3c) during which the difference between V_{int} and V_G changes from one steady state to another, and in this transition

period we have $|dV_{int}/dt| > |dV_G/dt|$, which indicates a differential internal voltage amplification ($\delta V_{int}/\delta V_G > 1$).

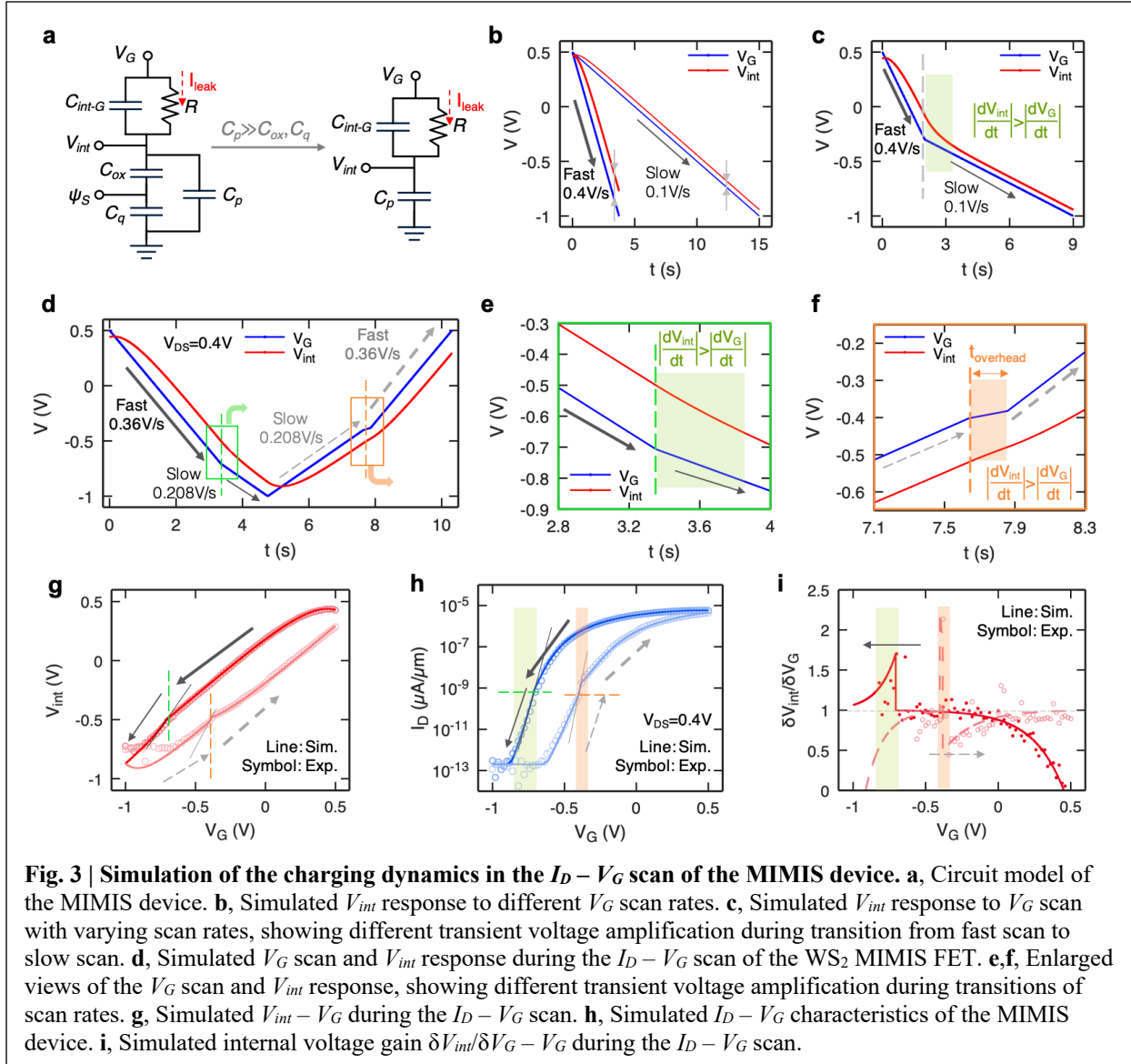
From the above analysis, it is clear that in the RC circuit model, differential internal voltage amplification occurs when the gate sweep rate is changed from “fast” to “slow”. Next, we identify such events in the experimental $I_D - V_G$ measurement of the WS₂ MIMIS device. When measuring the transfer characteristics of a transistor, since the current range may span more than 7 orders of magnitude (as shown in Figs. 2c & 2d), auto ranging is typically adopted by the semiconductor parameter analyzer³¹, and it is common to use slower scan rates for smaller current ranges to allow for longer integration times to reduce errors. On the other hand, faster scan rates are used for larger current ranges to increase measurement speed. In our measurement setup (see Methods), a “fast” scan rate of 0.36 V/s is adopted when the current level is above 1 nA (~ 0.6 nA/ μm in the $I_D - V_G$ curve, normalized by channel width $W=1.7$ μm), and a “slow” scan rate of 0.208 V/s is adopted when the current level is below 1 nA (Supplementary Section 2 and Supplementary Video 1).

Based on the findings, we reconstruct the V_G input as a function of time[†] during the $I_D - V_G$ scan of the WS₂ MIMIS device at $V_{DS} = 0.4$ V and simulate the V_{int} response based on Eq. (2), as shown in Fig. 3d. An initial condition $V_{int}(t = 0) = 0.43$ V is determined from the first datapoint in the measured $V_{int} - V_G$ shown in Fig. 2e. We monitor V_{int} and the respective I_D in the simulation and change the V_G sweep rate correspondingly when the current level reaches values above or below 1 nA to mimic the experimental setup. In the forward scan direction (0.5 V to -1 V) of the V_G sweep, we observe a differential internal voltage amplification when the V_G sweep rate changes from “fast” to “slow”, indicated by the green shaded area in Fig. 3e, which is in accordance with our previous analysis. In the backward scan direction

[†] In the real measurement, the V_G input should be a staircase function of time t , instead of a linear function used in the simulation. Yet due to the small step size (0.02 V), the difference is negligible.

(-1 V to 0.5 V), however, the scan rate change from “slow” to “fast” and should not result in the observed sub-60 mV/decade switching and differential voltage amplification shown in Figs. 2d & 2f. The reason for the observed phenomenon, i.e. again voltage amplification in the experiment, is that an overhead time $t_{overhead} \approx 0.22$ s is associated with the change of current measurement range[‡], as indicated by the orange shaded area in Fig. 3f. During the overhead time, V_G increases *only* by the scan step size $V_{step} = 0.02$ V, resulting in an equivalent scan rate of 0.091 V/s. Since dV_{int}/dt remains almost unchanged [Eq. (2)] while dV_G/dt slows down significantly during the overhead time, a transient differential internal voltage amplification $|dV_{int}/dt| > |dV_G/dt|$ occurs. Figs. 3g & 3h show the simulated internal gate voltage V_{int} and drain current I_D as a function of V_G , which shows good agreement with the experimental data. The experimentally observed characteristics, such as anti-clockwise hysteresis and sub-60 mV/decade switching in both sweeping directions, are reproduced in the simulation. The transition points of scan rates are indicated by the green and orange lines in the figures. Fig. 3i shows the simulated internal voltage gain $\delta V_{int}/\delta V_G$ as a function of V_G , which shows good agreement with the experimental data not only qualitatively, but also quantitatively in terms of amplitudes of the internal voltage amplifications and the corresponding V_G positions. This clearly shows that our simple model captures the essential characteristics of the charging dynamics of the $I_D - V_G$ measurement. Note that from Eq. (3), we can see that the voltage difference between V_{int} and V_G in the steady state is given by $RC_P \cdot (dV_G/dt)$, which is equal to 0.21 V and 0.12 V for “slow” and “fast” scan rates, respectively, and both are smaller than the voltage scan window of 1.5 V. If the RC time constant is too small, V_{int} would follow V_G completely; if the RC time constant is too large, V_{int} would not reach steady state within the voltage scan window. Therefore, the RC time constant needs to be comparable to the timescale of the V_G scan in order to see the described effects.

[‡] Although not specified in the manual of the semiconductor parameter analyzer³¹, our measurement results indicate that the overhead time only occurs at the transition from a smaller current measurement range into a larger measurement range, and not vice versa.



Simulation of sub-60 mV/decade switching with constant V_G scan rate. We have simulated the characteristics of the WS₂ MIMIS device with varying V_G scan rates and have shown that transient sub-60 mV/decade switching can be observed due to internal voltage amplifications when the scan rate is changing. However, one may argue that while varying scan rates are common when characterizing transistors, a constant scan rate is achievable with proper configuration of measurement setups and thus the effects discussed in the previous section can be avoided. To show that such effects are rather universal

and do not just apply to a particular scenario, we simulate the case of a constant V_G scan rate and show that sub-60 mV/decade switching can still be observed.

In the previous section, the circuit under discussion had a constant RC time constant due to a large, constant parasitic capacitance C_p , and in combination with a time-varying V_G scan rate, sub-60 mV/decade switching can be observed. One can envision that with a constant V_G scan rate, yet in combination with a *varying* RC time “constant”, similar effects could also be achieved. It is well-known that the gate capacitance of a MOSFET is voltage-dependent³², and for the 2D WS₂ transistor in this study, C_{MOS} can be represented by the series of oxide capacitance C_{ox} and quantum capacitance^{33,34} C_q , which can be expressed by:

$$C_q = q^2 \text{DOS}_{2D} f(E_C) A_{\text{device}} = q^2 \frac{g_C m_e^*}{\pi \hbar^2} \frac{1}{1 + \exp[(E_C - E_F)/k_B T]} A_{\text{device}} \quad (4)$$

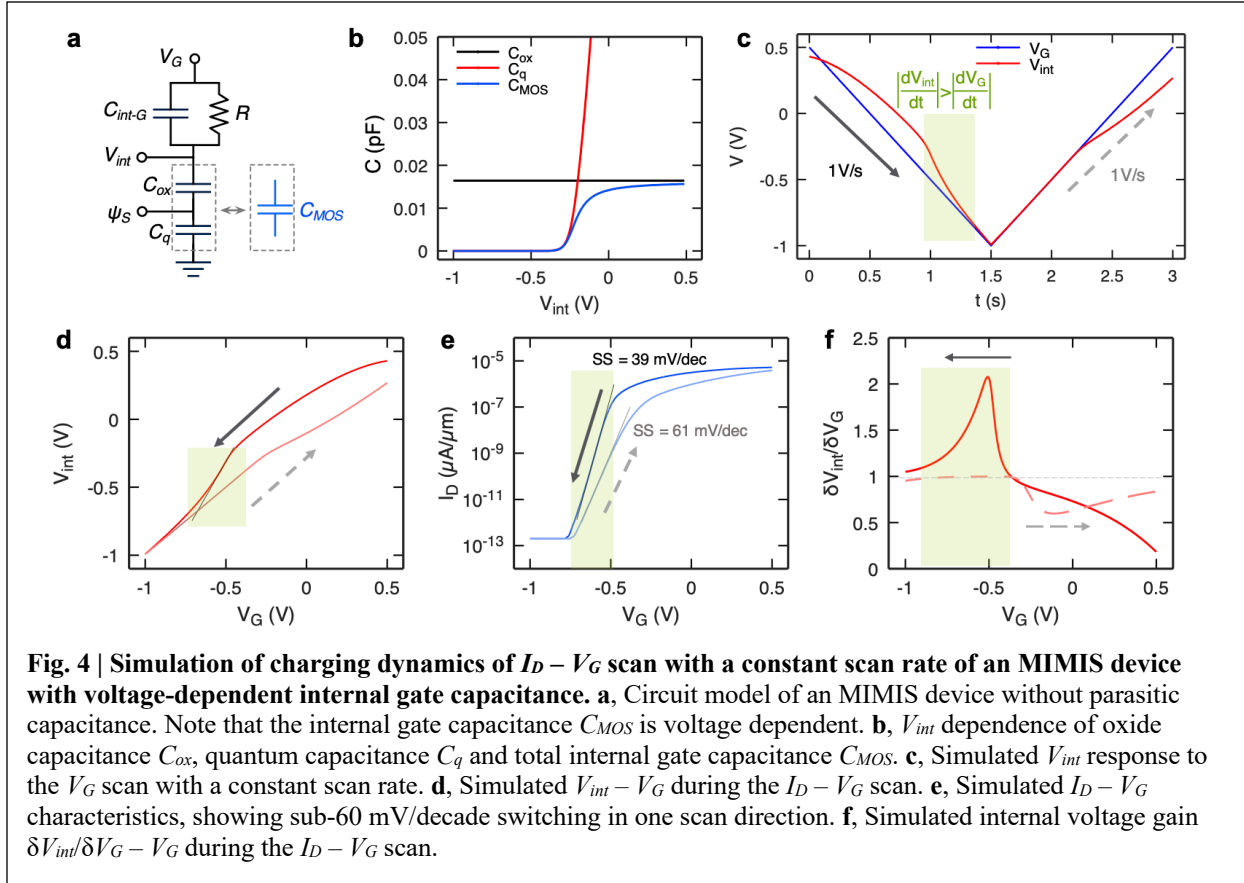
where g_C is conduction band valley degeneracy, m_e^* is electron effective mass. From Eq. (4), we can see that C_q is dependent on the relative position of conduction band edge E_C and Fermi level E_F , which can be tuned with gate voltage, and by removing the parasitic capacitance from the circuit, we can achieve a voltage-dependent internal gate capacitance C_{MOS} for the internal FET (Fig. 4a). Fig. 4b shows the simulated C_{ox} , C_q and C_{MOS} as a function of V_{int} (see Supplementary Section 3). One can see that when V_{int} is negative and the internal WS₂ FET is in its off-state, C_q is nearly zero as the Fermi level E_F in WS₂ is in the bandgap, and thus C_{MOS} is almost zero; when V_{int} increases and the internal WS₂ FET is turned on, C_q quickly increases and exceeds C_{ox} as the Fermi level E_F approaches the conduction band edge E_C , and thus C_{MOS} approaches C_{ox} .

Next, we simulate the V_{int} response with a constant V_G scan rate and voltage-dependent C_{MOS} , for which Eq. (1) and Eq. (2) are modified as follows:

$$\begin{aligned}
I_{\text{leak}} &= \frac{V_G - V_{\text{int}}}{R} = \frac{d}{dt} [Q_{\text{ch}}(V_{\text{int}}) - C_{\text{int-G}}(V_G - V_{\text{int}})] = \frac{\partial Q_{\text{ch}}}{\partial V_{\text{int}}} \frac{dV_{\text{int}}}{dt} - C_{\text{int-G}} \frac{d(V_G - V_{\text{int}})}{dt} \\
&= [C_{\text{MOS}}(V_{\text{int}}) + C_{\text{int-G}}] \frac{dV_{\text{int}}}{dt} - C_{\text{int-G}} \frac{dV_G}{dt}
\end{aligned} \tag{5}$$

$$\frac{dV_{\text{int}}}{dt} = \frac{V_G - V_{\text{int}}}{R[C_{\text{MOS}}(V_{\text{int}}) + C_{\text{int-G}}]} + \frac{C_{\text{int-G}}}{C_{\text{MOS}}(V_{\text{int}}) + C_{\text{int-G}}} \frac{dV_G}{dt} \tag{6}$$

From Eq. (6), we simulate the V_{int} response to the V_G scan with a constant scan rate of 1 V/s, as shown in Fig. 4c. We have also changed the parameter $R = 2 \times 10^{13} \Omega$ to compensate for the removal of a large capacitance C_p to keep the RC time constant approximately the same ($RC_{\text{ox}} = 0.32$ s). A differential internal voltage amplification $|dV_{\text{int}}/dt| > |dV_G/dt|$ (green shaded area) is observed in the forward scan direction (0.5 V to -1 V), but not in the backward scan direction (-1 V to 0.5 V). Fig. 4d shows the simulated V_{int} as a function of V_G . Assuming the same $I_D - V_{\text{int}}$ as in Fig. 2c, $I_D - V_G$ characteristics can be simulated (Fig. 4e), in which a sub-60 mV/decade switching is observed in the forward scan direction. Fig. 4f shows the simulated internal voltage gain $\delta V_{\text{int}}/\delta V_G$ as a function of V_G , in which the differential internal voltage amplification is clearly illustrated by the green shaded area.



Discussion

In previous demonstrations of NC-FETs, observing sub-60 mV/decade switching has been deemed as a mark of success for steep-slope switching devices. However, the results in this work show that by putting a leaky capacitor in series with the gate of an FET, which is clearly *not* a solution to steep-slope switching devices, sub-60 mV/decade switching can also be observed. Such effects originate from transient voltage amplifications over a small voltage window ($\delta V_{int}/\delta V_G > 1$), instead of persistent voltage amplifications over the entire voltage scan range ($\Delta V_{int}/\Delta V_G > 1$) that is required for a real demonstration of low-voltage switching. The transient voltage amplification may occur during transitions between current measurement ranges, where changes in the voltage scan rates are typical, and even for a constant scan rate, an abrupt change of internal gate capacitance near threshold voltage V_{th} may lead to similar effects. Since the effects are caused by the charging dynamics in a non-ideal measurement setup, which is likely to be utilized in

the characterization of NC-FETs by many, it is imperative to reassess the measurement setups in the previous reported sub-60 mV/decade switching NC-FETs with internal metal gates, to rule out such measurement-related artefacts and verify the existence of real voltage amplification predicted by the quasi-static NC theory.

Methods

Device fabrication

Internal gate electrodes (2 nm Ti) were deposited using e-beam evaporation onto a silicon substrate with 90 nm of silicon dioxide on top and patterned using standard e-beam lithography and lift-off process. 7 nm of HfO₂ was deposited using atomic layer deposition (ALD) on top of the internal gate metal as dielectric for the internal WS₂ FET. The HfO₂ film was grown using a low-temperature (90 °C) ALD process and patterned using e-beam lithography and lift-off to expose part of the internal gate metal. Few-layer WS₂ flakes were exfoliated onto the local bottom gate structure from bulk crystals (purchased from HQGraphene). Ni (40 nm) electrodes were deposited and patterned by e-beam evaporation and e-beam lithography as source/drain contacts for the WS₂ FET. A thin aluminium film was deposited on the exposed internal gate metal using e-beam evaporation and oxidized in air for 15 minutes to form the leaky AlO_x dielectric. To make sure the Al is fully oxidized, the evaporation-oxidization was done in two steps (evaporation-oxidation-evaporation-oxidation) with 2 nm Al in each deposition, instead of 4 nm in a single deposition step. Finally, the gate metal (40 nm Ti) was deposited using e-beam evaporation and patterned using e-beam lithography and lift-off process.

Device characterization

The electrical characterization was performed in a LakeShore FWPX Probe Station at a vacuum level below 10⁻⁵ Torr using an Agilent 4156C Parameter Analyzer. All measurements were performed at room temperature. The sweep measurement in the parameter analyzer has the following settings:

Primary sweep (VAR1): VG, start voltage: 0.5 V, end voltage: -1 V, step voltage: 0.02 V, double sweep: enabled, compliance: 1e-7 A

Subordinate sweep (VAR2): VD, start voltage: 0.1 V, step voltage: 0.3 V, no. of steps: 2, compliance: 1e-1 A

Measurement ranging mode: auto ranging, integration time: SHORT, hold time: 0.5 s, delay time: 0 s

Data availability:

The data that support the findings within this paper are available from the corresponding authors on reasonable request.

Code availability:

The computer code used in this study is available from the corresponding authors upon reasonable request.

References:

1. Salahuddin, S. & Datta, S. Use of negative capacitance to provide voltage amplification for low power nanoscale devices. *Nano Lett.* **8**, 405–410 (2008).
2. Kobayashi, M. A perspective on steep-subthreshold-slope negative-capacitance field-effect transistor. *Appl. Phys. Express* **11**, 110101 (2018).
3. Rethinking negative capacitance research. *Nat. Electron.* **3**, 503–503 (2020).
4. Hoffmann, M., Slesazek, S., Schroeder, U. & Mikolajick, T. What’s next for negative capacitance electronics? *Nat. Electron.* **3**, 504–506 (2020).
5. Rusu, A., Salvatore, G. A., Jimenez, D. & Ionescu, A. M. Metal-Ferroelectric-Meta-Oxide-semiconductor field effect transistor with sub-60mV/decade subthreshold swing and internal voltage amplification. in *2010 International Electron Devices Meeting* 16.3.1-16.3.4 (IEEE, 2010). doi:10.1109/IEDM.2010.5703374
6. McGuire, F. A. *et al.* Sustained Sub-60 mV/decade switching via the negative capacitance effect in MoS₂ Transistors. *Nano Lett.* **17**, 4801–4806 (2017).
7. Si, M. *et al.* Sub-60 mV/dec ferroelectric HZO MoS₂ negative capacitance field-effect transistor with internal metal gate: The role of parasitic capacitance. in *2017 IEEE International Electron Devices Meeting (IEDM)* 23.5.1-23.5.4 (IEEE, 2017). doi:10.1109/IEDM.2017.8268447
8. Si, M. *et al.* Steep-Slope WSe₂ Negative Capacitance Field-Effect Transistor. *Nano Lett.* **18**, 3682–3687 (2018).
9. Saeidi, A. *et al.* Near Hysteresis-Free Negative Capacitance InGaAs Tunnel FETs with Enhanced Digital and Analog Figures of Merit below V_{DD}=400mV. in *2018 IEEE International Electron Devices Meeting (IEDM)* 13.4.1-13.4.4 (IEEE, 2018). doi:10.1109/IEDM.2018.8614583
10. Krivokapic, Z. *et al.* 14nm Ferroelectric FinFET technology with steep subthreshold slope for ultra low power applications. in *2017 IEEE International Electron Devices Meeting (IEDM)* 15.1.1-15.1.4 (IEEE, 2017). doi:10.1109/IEDM.2017.8268393
11. Cao, W. & Banerjee, K. Is negative capacitance FET a steep-slope logic switch? *Nat. Commun.*

- 11**, (2020).
12. Liu, Z., Bhuiyan, M. A. & Ma, T. P. A Critical Examination of ‘Quasi-Static Negative Capacitance’ (QSNC) theory. in *2018 IEEE International Electron Devices Meeting (IEDM)* 31.2.1-31.2.4 (IEEE, 2018). doi:10.1109/IEDM.2018.8614614
 13. Kittl, J. A. *et al.* On the validity and applicability of models of negative capacitance and implications for MOS applications. *Appl. Phys. Lett.* (2018). doi:10.1063/1.5036984
 14. Li, X. & Toriumi, A. Direct relationship between sub-60 mV/dec subthreshold swing and internal potential instability in MOSFET externally connected to ferroelectric capacitor. in *2018 IEEE International Electron Devices Meeting (IEDM)* 31.3.1-31.3.4 (IEEE, 2018). doi:10.1109/IEDM.2018.8614703
 15. Li, X. & Toriumi, A. Stepwise internal potential jumps caused by multiple-domain polarization flips in metal/ferroelectric/metal/paraelectric/metal stack. *Nat. Commun.* **11**, 1895 (2020).
 16. Han, Q. *et al.* Transient negative capacitance and charge trapping in FDSOI MOSFETs with ferroelectric HfYO_x. *Solid. State. Electron.* **159**, 71–76 (2019).
 17. Chang, S.-C., Avci, U. E., Nikonov, D. E., Manipatruni, S. & Young, I. A. Physical Origin of Transient Negative Capacitance in a Ferroelectric Capacitor. *Phys. Rev. Appl.* **9**, 014010 (2018).
 18. Saha, A. K., Datta, S. & Gupta, S. K. “Negative capacitance” in resistor-ferroelectric and ferroelectric-dielectric networks: Apparent or intrinsic? *J. Appl. Phys.* **123**, 105102 (2018).
 19. Wang, H. *et al.* New Insights into the Physical Origin of Negative Capacitance and Hysteresis in NCFETs. in *2018 IEEE International Electron Devices Meeting (IEDM)* 31.1.1-31.1.4 (IEEE, 2018). doi:10.1109/IEDM.2018.8614504
 20. Jin, C., Saraya, T., Hiramoto, T. & Kobayashi, M. Transient Negative Capacitance as Cause of Reverse Drain-induced Barrier Lowering and Negative Differential Resistance in Ferroelectric FETs. in *2019 Symposium on VLSI Technology* T220–T221 (IEEE, 2019). doi:10.23919/VLSIT.2019.8776583
 21. Jin, C., Jang, K., Saraya, T., Hiramoto, T. & Kobayashi, M. Experimental Study on the Role of

- Polarization Switching in Subthreshold Characteristics of HfO₂-based Ferroelectric and Anti-ferroelectric FET. in *2018 IEEE International Electron Devices Meeting (IEDM)* 31.5.1-31.5.4 (IEEE, 2018). doi:10.1109/IEDM.2018.8614486
22. Obradovic, B., Rakshit, T., Hatcher, R., Kittl, J. A. & Rodder, M. S. Modeling Transient Negative Capacitance in Steep-Slope FeFETs. *IEEE Trans. Electron Devices* **65**, 5157–5164 (2018).
 23. Khan, A. I. *et al.* Negative capacitance in a ferroelectric capacitor. *Nat. Mater.* **14**, 182–186 (2015).
 24. Hoffmann, M. *et al.* Unveiling the double-well energy landscape in a ferroelectric layer. *Nature* **565**, 464–467 (2019).
 25. Kim, Y. J. *et al.* Voltage Drop in a Ferroelectric Single Layer Capacitor by Retarded Domain Nucleation. *Nano Lett.* **17**, 7796–7802 (2017).
 26. Song, S. J. *et al.* Alternative interpretations for decreasing voltage with increasing charge in ferroelectric capacitors. *Sci. Rep.* **6**, 1–6 (2016).
 27. Khan, A. I., Radhakrishna, U., Chatterjee, K., Salahuddin, S. & Antoniadis, D. A. Negative Capacitance Behavior in a Leaky Ferroelectric. *IEEE Trans. Electron Devices* **63**, 4416–4422 (2016).
 28. Khan, A. I., Radhakrishna, U., Salahuddin, S. & Antoniadis, D. Work Function Engineering for Performance Improvement in Leaky Negative Capacitance FETs. *IEEE Electron Device Lett.* **38**, 1335–1338 (2017).
 29. Scott, J. F. Ferroelectrics go bananas. *J. Phys. Condens. Matter* **20**, 021001 (2008).
 30. Pang, C.-S., Wu, P., Appenzeller, J. & Chen, Z. Sub-1nm EOT WS₂-FET with I_{DS} > 600μA/μm at V_{DS}=1V and SS < 70mV/dec at L_G=40nm. in *2020 IEEE International Electron Devices Meeting (IEDM)* 3.4.1-3.4.4 (IEEE, 2020).
 31. *Agilent 4155C/4156C Semiconductor Parameter Analyzer, User's Guide Vol. 2, Measurement & Analysis.* Agilent Technologies (2003).
 32. Sze, S. M. & Ng, K. K. *Physics of Semiconductor Devices.* Physics of Semiconductor Devices

(2006). doi:10.1002/0470068329

33. John, D. L., Castro, L. C. & Pulfrey, D. L. Quantum capacitance in nanoscale device modeling. *J. Appl. Phys.* **96**, 5180–5184 (2004).
34. Ma, N. & Jena, D. Carrier statistics and quantum capacitance effects on mobility extraction in two-dimensional crystal semiconductor field-effect transistors. *2D Mater.* **2**, 015003 (2015).

Acknowledgements:

This work was supported in part by the Semiconductor Research Corporation (SRC) at the NEW LIMITS Center and National Institute of Standards and Technology (NIST) through award number 70NANB17H041

Author contributions:

P.W. and J.A. conceived the idea and designed the experiments. P.W. performed the device fabrication, characterization and the simulation. Both authors wrote the manuscript.

Competing interests:

The authors declare no competing interests.

Additional information:

Correspondence and requests for materials should be addressed to P.W. and J.A.

Supplementary Information for

**Sub-60 mV/decade switching in a metal-insulator-metal-insulator-semiconductor transistor
without ferroelectric component**

Peng Wu^{1,2}, Joerg Appenzeller^{1,2*}*

¹Birck Nanotechnology Center, Purdue University, West Lafayette, Indiana 47907, USA

²Department of Electrical and Computer Engineering, Purdue University, West Lafayette, Indiana 47907,
USA

*E-mail: wu936@purdue.edu, appenzeller@purdue.edu

1. Determination of capacitance and resistance components in the RC network model

Supplementary Fig. 1a shows a schematic of the capacitance and resistance components in the WS₂ MIMIS device. The overlapping area of internal gate and gate is $A_{int-G} = 1 \mu\text{m}^2$ and the area of the contact pad for the internal gate is $A_{pad} = 50 \mu\text{m} \times 50 \mu\text{m} = 2500 \mu\text{m}^2$, respectively. The device area of the WS₂ FET is $A_{device} = 1 \mu\text{m}^2$. The capacitances can be calculated:

$$C_{int-G} = \frac{\varepsilon_{\text{AlO}_x} \varepsilon_0 A_{int-G}}{t_{\text{AlO}_x}} = \frac{7 \times 8.854 \times 10^{-12} \times 1 \times (10^{-6})^2}{8 \times 10^{-9}} = 7.75 \times 10^{-15} \text{ F} \quad (1)$$

$$C_p = \frac{\varepsilon_{\text{SiO}_2} \varepsilon_0 A_{pad}}{t_{\text{SiO}_2}} = \frac{3.9 \times 8.854 \times 10^{-12} \times (50 \times 10^{-6})^2}{90 \times 10^{-9}} = 9.59 \times 10^{-13} \text{ F} \quad (2)$$

$$C_{ox} = \frac{\varepsilon_{\text{HfO}_2} \varepsilon_0 A_{device}}{t_{\text{HfO}_2}} = \frac{13 \times 8.854 \times 10^{-12} \times (1 \times 10^{-6})^2}{7 \times 10^{-9}} = 1.64 \times 10^{-14} \text{ F} \quad (3)$$

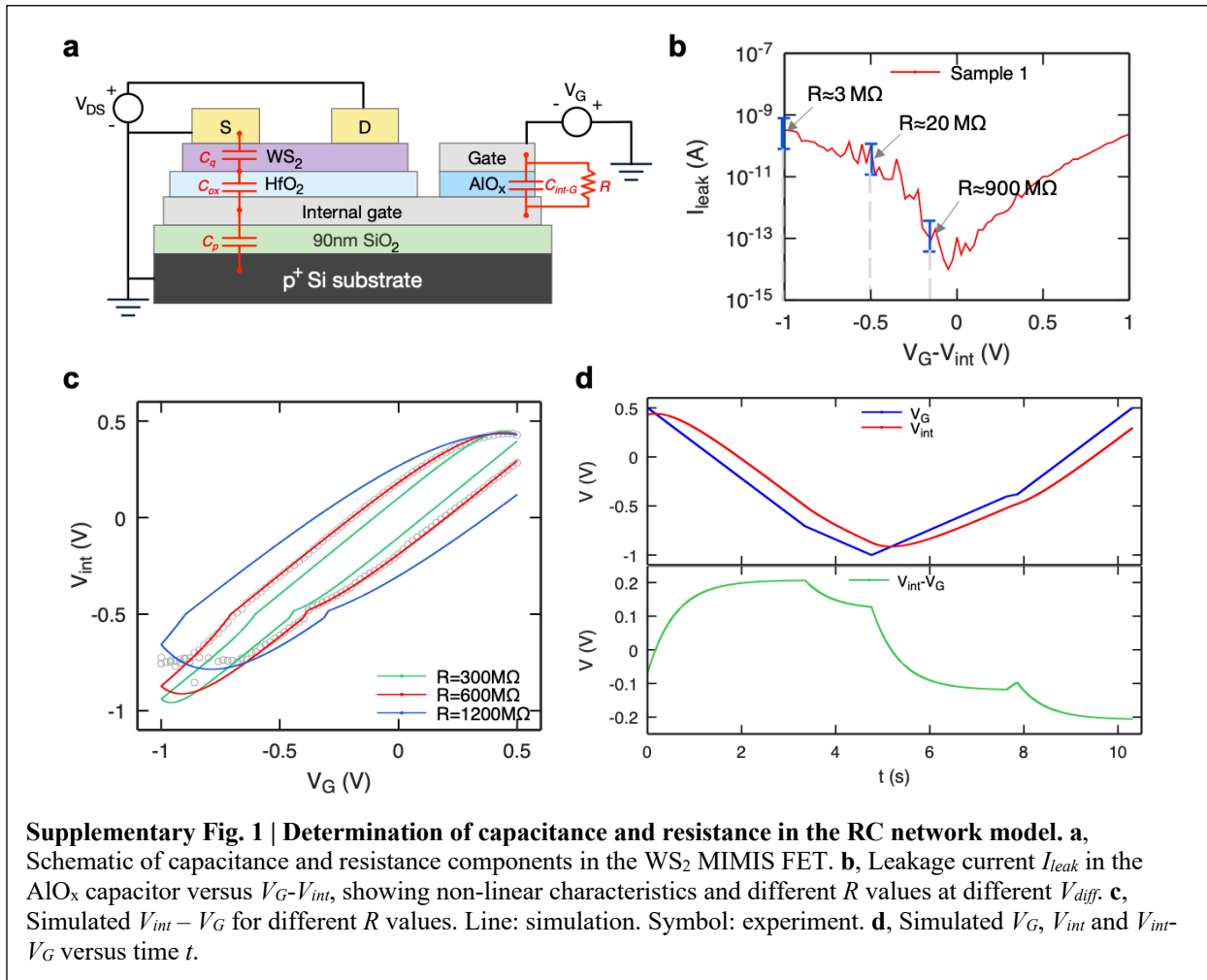
The calculation of C_q can be found in Supplementary Section 3, yet since it's in series with C_{ox} , the total capacitance C_{MOS} is smaller than C_{ox} . We can see that C_{ox} is much smaller than C_p . Therefore, we can ignore C_{MOS} when simulating the V_{int} response.

Next, the resistance value for R is determined. Supplementary Fig. 1b shows the leakage current I_{leak} in the AlO_x capacitor as a function of voltage difference $V_{diff} = V_G - V_{int}$, which clearly exhibits a non-linear behavior and different R values can be extracted at different V_{diff} -values. In addition, due to inaccuracies and noises in the measurement, there is a significant uncertainty associated with the extracted R value, especially when the current is small. Therefore, we have adopted an indirect method of extracting R by fitting the measured $V_{int} - V_G$ curve, as shown in Supplementary Fig. 1c. We have derived in the main text that, in the steady state:

$$V_G - V_{int} = R C_p \frac{dV_G}{dt} \quad (4)$$

Therefore, different R values lead to different $V_G - V_{int}$ values and thus different hysteresis voltage values in the bidirectional V_G scan. As clearly shown in Supplementary Fig. 1c, $R = 600 \text{ M}\Omega$ gives the best fit to

the experimental data, while other values either underestimate or overestimate the hysteresis voltage. The good fitting also indicates that using a fixed value for R is a good approximation despite the non-linear $I_{leak} - V_{diff}$ characteristics. Supplementary Fig. 1d shows the simulated $V_{int} - V_G$ as a function of time using the parameter $R = 600 \text{ M}\Omega$. The voltage difference is below 0.21 V during the V_G voltage scan, and from the $I_{leak} - V_{diff}$ characteristics in Supplementary Fig 1b, we can roughly estimate $R \approx 900 \text{ M}\Omega$ at $V_G - V_{int} = -0.2 \text{ V}$, which is in acceptable agreement with the extracted $R = 600 \text{ M}\Omega$.

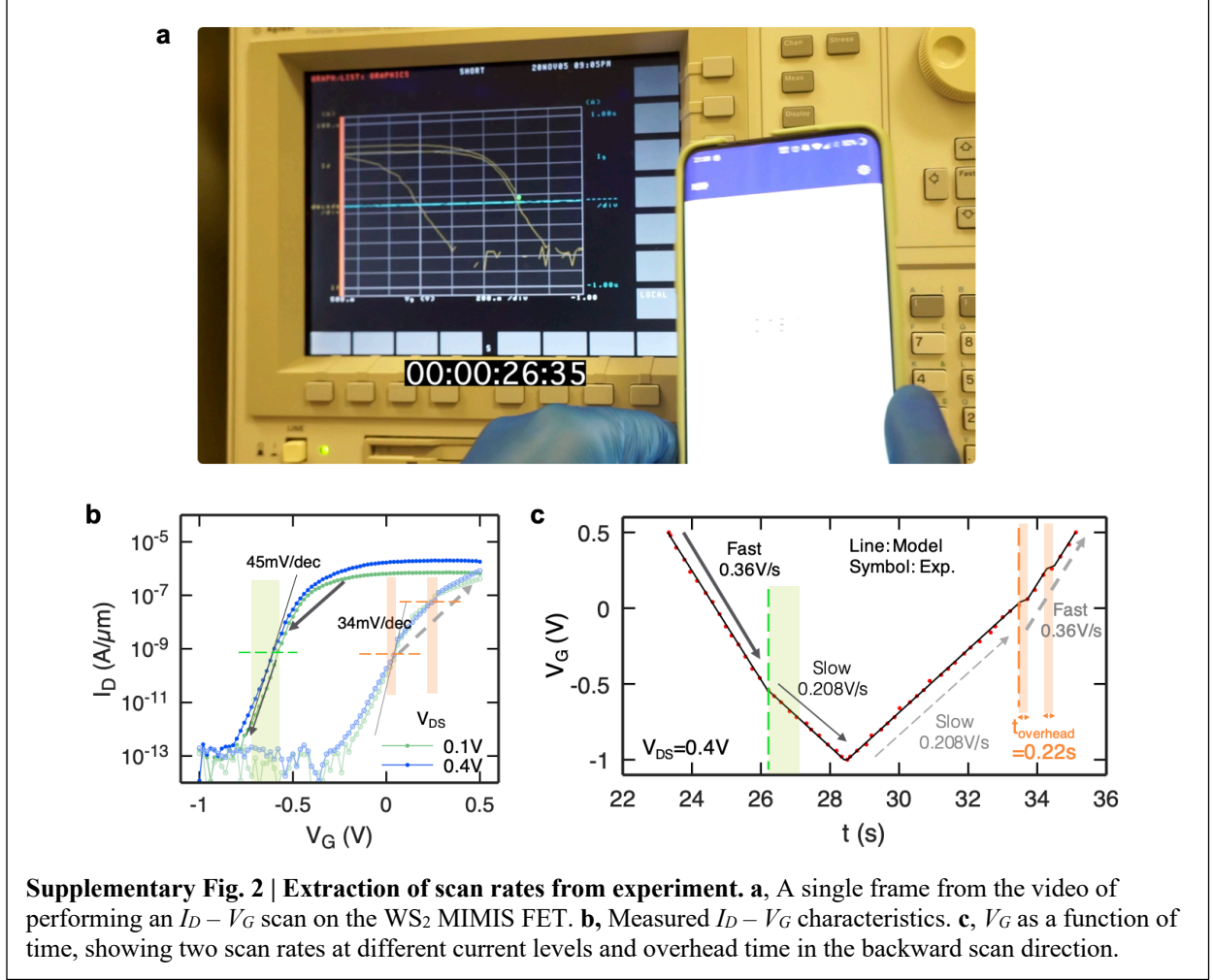


2. Extraction of scan rates from experiment

Supplementary Video 1 shows a video of a researcher performing an $I_D - V_G$ scan of the WS₂ MIMIS FET on the Agilent 4156C parameter analyzer (a single frame of the video is shown in Supplementary Fig. 2a as an example). The measured $I_D - V_G$ characteristics are shown in Supplementary Fig. 2b. Note that the

measurement was performed ~ 3 months after the initial measurement (Fig. 2d in the main text), and the characteristics have drifted slightly compared to the initial characterization. In particular, the hysteresis voltage had become larger, which indicates an increase in the resistance R of the AlO_x capacitor according to our analysis from the previous section. However, the main features, such as sub-60 mV/decade switching and anti-clockwise hysteresis, are still retained in the new measurement.

From the video, we extract the gate voltage V_G as a function of time t for $V_{DS} = 0.4$ V, as shown by the red dots in Supplementary Fig. 2c. It is clear that two distinct scan rates of 0.36 V/s (“fast”) and 0.208 V/s (“slow”) can be extracted from the measured $V_G - t$ curve, which correspond to I_D above and below 1 nA (0.6 nA/ μm), respectively. The values for the “fast” and “slow” scans are applied in the simulation for the V_{int} response in the main text. In the forward scan direction (0.5 V to -1 V), sub-60 mV/decade switching is observed when the scan rate transitions from “fast” to “slow” at $I_D = 1$ nA (green shaded area). In the backward scan (-1 V to 0.5 V), two sub-60 mV/decade switching events are observed, one at $I_D = 1$ nA and another at $I_D = 100$ nA, which correspond to the overhead time associated with two measurement range changes, as shown by the orange shaded areas in Supplementary Fig. 2c. Interestingly, the second sub-60 mV/decade event at $I_D = 100$ nA was not observed in the initial measurement. The cause for the difference is still under investigation, which we speculate might be from some minor changes in the settings of the parameter analyzer in the initial measurement and the new measurement, despite our effort of making them the same.



3. Calculation of quantum capacitance C_q

Supplementary Fig. 3a shows the schematic of the capacitance model for the WS₂ internal FET. The quantum capacitance C_q of 2D WS₂ channel is given by:

$$C_q = \frac{\partial Q_{\text{ch}}}{\partial \psi_S} = q^2 \text{DOS}_{2\text{D}} f(E_C) A_{\text{device}} = q^2 \frac{g_C m_e^*}{\pi \hbar^2} \frac{1}{1 + \exp\left(\frac{E_C - E_F}{k_B T}\right)} A_{\text{device}} \quad (5)$$

Eq. (5) describes the dependence of C_q on the relative position of E_C and Fermi level E_F , or equivalently the surface potential ψ_S . In order to calculate the V_{int} dependence of C_q , we need to determine the relation of ψ_S and V_{int} , which is given by:

$$\frac{d\psi_S}{dV_{\text{int}}} = \frac{C_{\text{ox}}}{C_{\text{ox}} + C_q} \quad (6)$$

$$\psi_S = \frac{\Phi_{SB,n} + E_F - E_C}{q} \quad (7)$$

Note that we have chosen flat-band condition as the zero point for the potential ψ_S , i.e., $\psi_S = 0$ when $V_{int} = V_{FB}$. For multilayer WS_2 in this study, we have:

$$g_C = 6, m_e^* = 0.22 m_0$$

The only missing parameters are the flat-band voltage V_{FB} and electron Schottky barrier height $\Phi_{SB,n}$. We extract these parameters by fitting experimental $I_D - V_{int}$ data with a Landauer model^{1,2}, as shown in Supplementary Fig. 3b. Using the Landauer model, we extract the parameters:

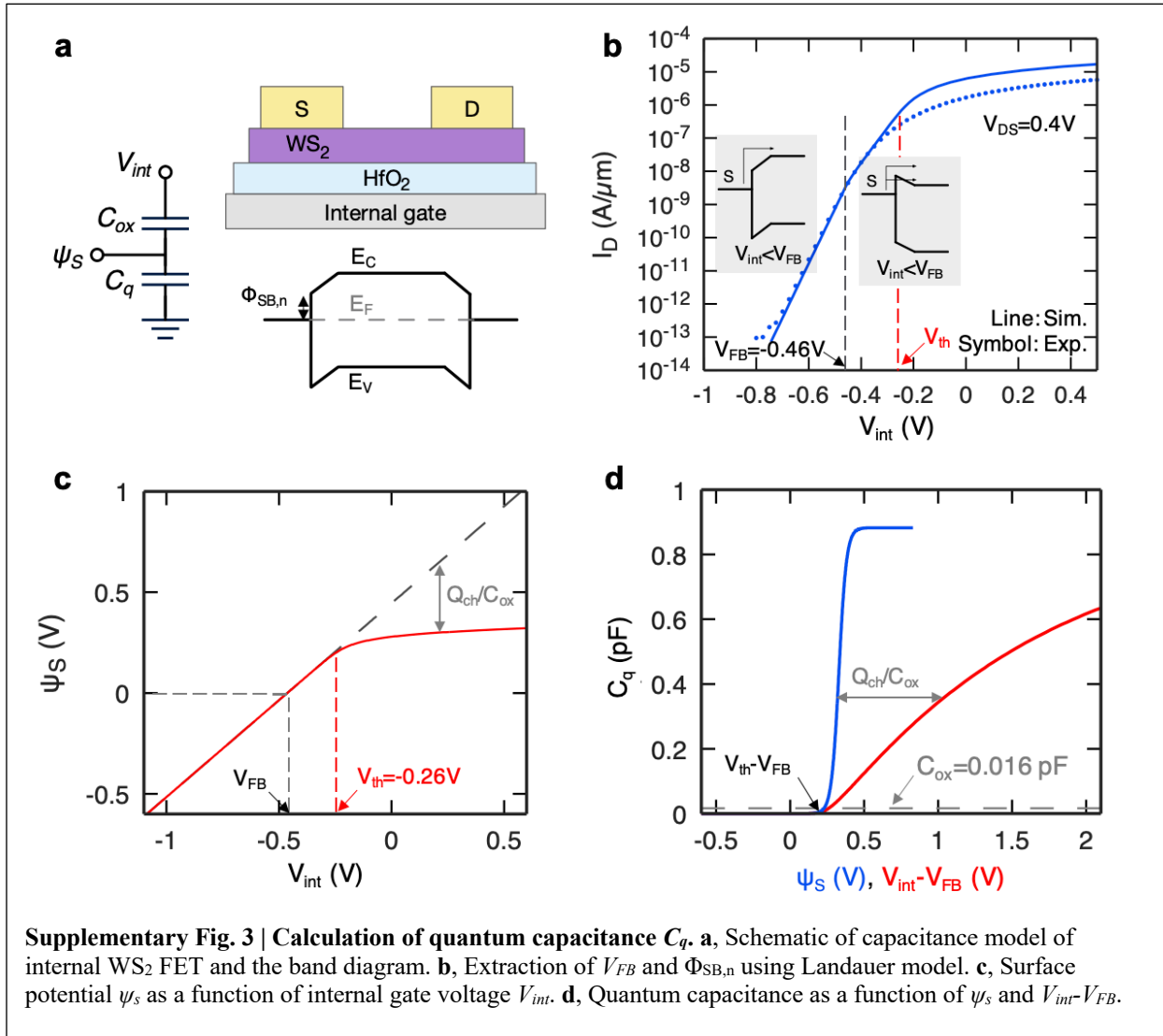
$$V_{FB} = -0.46 \text{ V}, \Phi_{SB,n} = 0.33 \text{ eV},$$

and the screening length for Schottky barrier injection $\lambda = 2.6 \text{ nm}$. Notice that above V_{th} (the extraction of its value will be discussed next), the simulated curve from Landauer model starts to deviate from experimental data. This is because the Landauer approach is based on a ballistic transport picture, while above V_{th} , electrons start to populate the channel and a diffusive picture should be adopted for the long channel device ($L \approx 0.6 \mu\text{m}$) in this study. However, the fitting for the data below V_{th} , where scattering can be ignored, is already sufficient to extract the critical parameters and we did not try to simulate the on-state of the device quantitatively.

Having determined the values of V_{FB} and $\Phi_{SB,n}$, we calculate ψ_S as a function of V_{int} based on Eqs. (6-7), as shown in Supplementary Fig. 3c. One can see that ψ_S is following V_{int} one-to-one below $V_{th} = -0.26 \text{ V}$. Above V_{th} , channel charges Q_{ch} become significant and ψ_S starts to saturate and deviate from the one-to-one relation.

Finally, we calculate C_q as a function of ψ_S based on Eq. (5), as shown by the blue line in Supplementary Fig. 3d. One would expect C_q to show up as a step function of ψ_S at $T = 0 \text{ K}$, yet at finite temperatures, the transition becomes more gradual due to thermal broadening. By applying the $\psi_S - V_{int}$ relation shown in Supplementary Fig. 3c, we can determine C_q as a function of V_{int} , as shown by the red line in

Supplementary Fig. 3d. Note that $C_{q,max} \gg C_{ox}$, which indicates C_{MOS} , the series capacitance of C_{ox} and C_q , will quickly saturate to C_{ox} once V_{int} is above V_{th} , as shown in Fig. 4b in the main text.



References:

1. Penumatcha, A. V., Salazar, R. B. & Appenzeller, J. Analysing black phosphorus transistors using an analytic Schottky barrier MOSFET model. *Nat. Commun.* **6**, 8948 (2015).
2. Appenzeller, J., Zhang, F., Das, S. & Knoch, J. *Transition Metal Dichalcogenide Schottky Barrier Transistors – A Device Analysis and Material Comparison*, Chapter 8, pp. 207-240 in *2D Materials for Nanoelectronics*, (Editors: M. Houssa, T. Dimoulas and A. Molle), Taylor and Francis (2016).